ACS NANO
Cite This: ACS Nano 2018, 12, 2193−2200
www.acsnano.org

ARTICLE

# Hierarchical On-Surface Synthesis of Graphene Nanoribbon Heterojunctions

Christopher Bronner,*[,†,#] Rebecca A. Durr,[‡,#] Daniel J. Rizzo,[†] Yea-Lee Lee,[†,§] Tomas Marangoni,[‡] Alin Miksi Kalayjian,[‡] Henry Rodriguez,[†] William Zhao,[†] Steven G. Louie,[†,∥] Felix R. Fischer,*[,‡,∥,⊥] and Michael F. Crommie*[,†,∥,⊥]

[†]Department of Physics, University of California, Berkeley, California 94720, United States
[‡]Department of Chemistry, University of California, Berkeley, California 94720, United States
[§]Department of Physics, Pohang University of Science and Technology, Pohang, Kyungbuk 37673, Korea
[∥]Materials Sciences Division, Lawrence Berkeley National Laboratory, Berkeley, California 94720, United States
[⊥]Kavli Energy NanoSciences Institute at the University of California Berkeley and the Lawrence Berkeley National Laboratory, Berkeley, California 94720, United States

Supporting Information

**ABSTRACT:** **Bottom-up graphene nanoribbon (GNR) heterojunctions are nanoscale strips of graphene whose electronic structure abruptly changes across a covalently bonded interface. Their rational design offers opportunities for profound technological advancements enabled by their extraordinary structural and electronic properties. Thus far, the most critical aspect of their synthesis, the control over sequence and position of heterojunctions along the length of a ribbon, has been plagued by randomness in monomer sequences emerging from step-growth copolymerization of distinct monomers. All bottom-up GNR heterojunction structures created so far have exhibited random sequences of heterojunctions and, while useful for fundamental scientific studies, are difficult to incorporate into functional nanodevices as a result. In contrast, we describe a hierarchical fabrication strategy that allows the growth of bottom-up GNRs that preferentially exhibit a single heterojunction interface rather than a random statistical sequence of junctions along the ribbon. Such heterojunctions provide a viable platform that could be directly used in functional GNR-based device applications at the molecular scale. Our hierarchical GNR fabrication strategy is based on differences in the dissociation energies of C−Br and C−I bonds that allow control over the growth sequence of the block copolymers from which GNRs are formed and consequently yields a significantly higher proportion of single-junction GNR heterostructures. Scanning tunneling spectroscopy and density functional theory calculations confirm that hierarchically grown heterojunctions between chevron GNR (cGNR) and binaphthyl-cGNR segments exhibit straddling Type I band alignment in structures that are only one atomic layer thick and 3 nm in width.**


**KEYWORDS:** *graphene nanoribbon, on-surface synthesis, heterojunction, hierarchical growth, bottom-up fabrication, electronic structure*

Functional GNRs are attractive candidates for high-speed digital nanodevices because they develop sizable bandgaps (*e.g.*, 1−3 eV) as their widths become small (*e.g.*, 1−3 nm).[1−5] For example, GNR-based heterojunctions could be employed in devices such as molecular-scale tunneling field effect transistors and resonant tunneling diodes.[6−9] The extreme sensitivity of GNR electrical properties to minute structural variations,[1−5,10] however, requires that practical GNR heterojunctions must have feature sizes that are well-controlled at the atomic scale. While this represents an insurmountable challenge for current top-down fabrication techniques,[11−14] it is actually routine practice using molecular assembly-based bottom-up techniques that involve on-surface polymerization of molecular precursors followed by cyclodehydrogenation.[15−22] Atomically precise bottom-up GNR heterojunctions have been synthesized previously in this way by combining molecular precursors that have different heteroatom doping patterns[23] (leading to dopant-induced heterojunctions) or different widths[24] (leading to width-based heterojunctions). GNR heterojunctions have also been fabricated from a single molecular precursor designed with sacrificial ligands that can be removed or chemically altered after growth to create abrupt variations in bandgap profile along the GNR axis.[25,26] The number and placement of all such heterojunctions, however, has so far been random due to the stochastic nature of thermally driven molecular step growth polymerization, a

Received: December 6, 2017
Accepted: January 30, 2018
Published: January 30, 2018






DOI: 10.1021/acsnano.7b08658
ACS Nano 2018, 12, 2193−2200

situation that is problematic for the design, reproducibility, and ultimately implementation of functional GNR heterojunction nanodevices.

Hierarchical growth provides a potential solution to this problem as it provides an additional level of control to the bottom-up synthesis approach.[27,28] This arises from the fact that a careful selection of molecular building blocks can lead to a sequential activation of the growth process at different temperatures. Thermally driven GNR self-assembly is still a random process even under hierarchical growth conditions, but *different molecules* are induced to polymerize at *different temperatures*, thus providing an added element of control. For example, if a first GNR assembles (*i.e.*, polymerizes) at temperature $T_1$ and a second GNR assembles at temperature $T_2 > T_1$, then by ramping the temperature it should be possible to grow a heterojunction between both GNRs that has only a single interface rather than the stochastic interfaces expected from a mixture of different precursors that polymerize at the same temperature. There are three elements needed to successfully achieve this hierarchical growth process: (i) precursor molecules for the first GNR that can be activated at $T_1$, (ii) precursor molecules for the second GNR that polymerize at $T_2 > T_1$, and (iii) a linker molecule that facilitates growth of the second GNR off the end of the first GNR. Our strategy for accomplishing this hierarchical growth relies on functionalizing the first GNR precursors with iodine and the second GNR precursors with bromine. Because the C–I bond is weaker than the C–Br bond,[29−33] this ensures that $T_2 > T_1$ (due to the fact that GNR polymerization does not occur until thermally driven dehalogenation causes precursors to become reactive radicals). Our linker elements are precursors of the second GNR that are functionalized on one side with iodine and on the other side with bromine groups. A related strategy has been developed previously to facilitate the growth of 2D polymer networks, but with no heterojunction functionality.[27,28]

## HIERARCHICAL ON-SURFACE SYNTHESIS OF CONTROLLED GNR HETEROJUNCTIONS

For the hierarchical growth demonstrated here, the first GNR was chosen to be the well-known chevron GNR[15,23,34−36] (cGNR), whereas the second GNR is a laterally extended chevron structure (binaphthyl-cGNR (binaph-cGNR)) that was designed to have a wider spatial profile specifically for this study. The chosen linker element possesses the same structure as binaph-cGNR. Figure 1 shows the reaction of the iodinated precursor **1** that gives rise to the cGNR, the dual-functionalized linker precursor **2**, and the brominated precursor **3** that gives rise to the binaph-cGNR. At the lower polymerization temperature ($T_1$), only the C–I bond in **2** will be activated, and the linker molecule will effectively terminate the growth of homopolymers of **1** (Figure 1b). At $T_2$ the C–Br bond in **2** can be cleaved and serves as a seed for the polymerization of **3** (Figure 1c). Precursor **3** will induce polymerization of the wider binaph-cGNR segment at temperatures higher than those required for the polymerization of the iodinated precursors **1** and **2**. GNR heterojunctions arising after cyclodehydrogenation of the block copolymers arising from this process at $T_3$ are expected to show type I band alignment due to the smaller bandgap that arises from the wider binaphthyl-GNR segment.

The synthesis of **1** has been reported elsewhere.[37,36] Precursor **2** was obtained through monoiodination of 9,10-phenanthrenequinone followed by bromination to yield 2-bromo-7-iodophenanthrene-9,10-dione in 13% yield. Knoevenagel condensation with 1,3-diphenyl acetone followed by a Diels–Alder reaction with 2-ethynyl-1,1′-binaphthalene (**6**) afforded **2** in 47% yield as an inseparable 1:1 mixture of regioisomers with respect to the position of the I/Br substituents at the C6/C11 position of the triphenylene core (Figure 2a). Precursor **3** was prepared from 2,7-dibromophe-

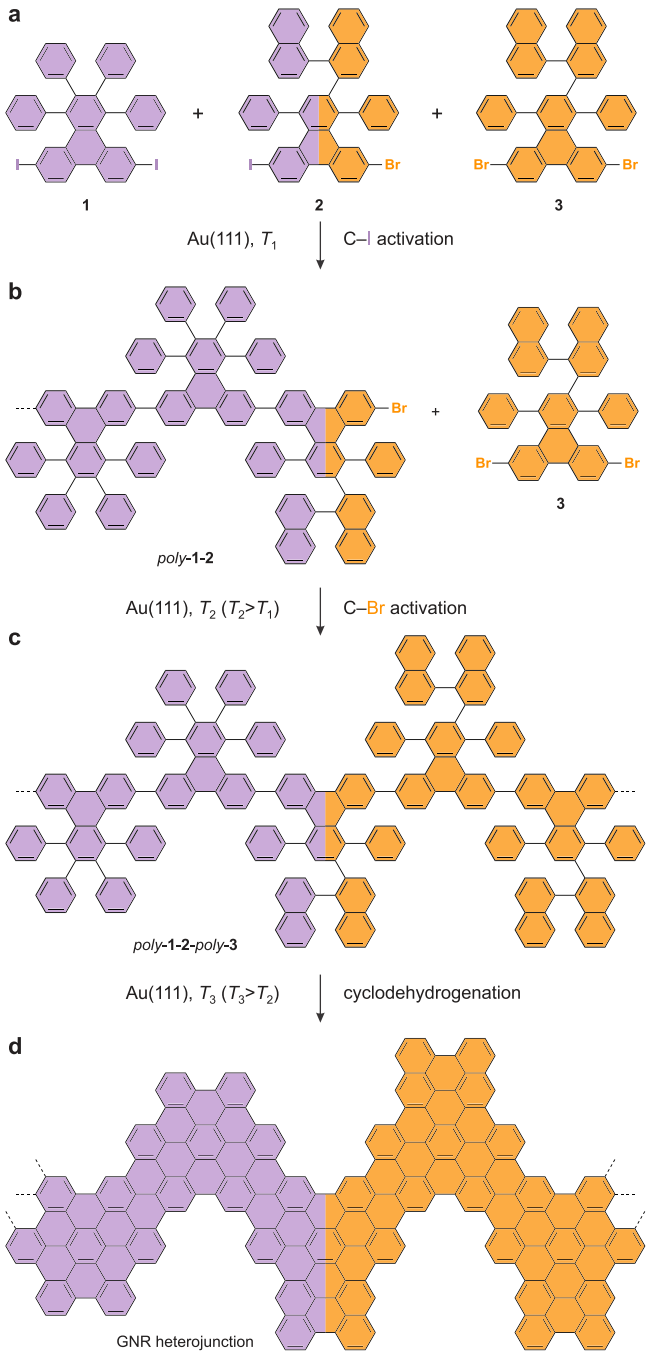


**Figure 1. Schematic representation of the hierarchical on-surface synthesis of GNR heterojunctions. (a) Molecular precursors 1, 2, and 3. (b) Selective activation of the C–I bonds at $T_1$ leads to *poly*-1-2 terminated by the bifunctional linker 2. C–Br bonds in 2 and 3 are not activated at $T_1$. (c) Selective activation of the C–Br bonds at $T_2$ results in a block copolymer consisting of *poly*-1 and *poly*-3 segments fused by the linker 2. (d) Cyclodehydrogenation at $T_3$ yields a GNR heterojunction between fully cyclized cGNR and binaph-cGNR segments.**



DOI: 10.1021/acsnano.7b08658
*ACS Nano* 2018, 12, 2193−2200

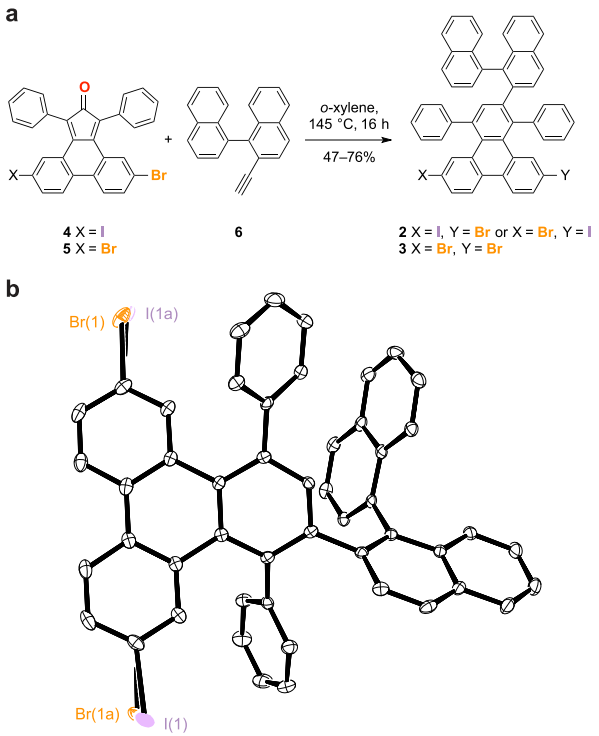


**Figure 2. Synthesis of bifunctional linker 2 and binaph-cGNR precursor 3. (a) Synthesis of linker 2 and binaph-cGNR precursor 3. (b) ORTEP representation of the X-ray crystal structure of 2. Thermal ellipsoids are drawn at the 50% probability level. Color coding: C (gray), Br (orange), I (purple). 2 crystallizes as a 1:1 mixture of regioisomers with respect to the position of the I/Br substituent at the C6/C11 position of the triphenylene core. Hydrogen atoms are omitted for clarity.**

nanthrene-9,10-dione in two steps in 76% yield. $^1$H NMR of analytically pure samples of **2** and **3** at 24 °C reveals a complex spectrum attributed to the slow interconversion of rotational isomers around the binaphthyl group. Variable-temperature NMR of both **2** and **3** in 1,1,2,2-tetrachloroethane-d2 at 110 °C resolves the spectroscopic signals (Supporting Information Figures S6 and S7). Pale yellow crystals of **2** suitable for X-ray diffraction were grown from saturated $CHCl_3$/MeOH solutions. In the crystal structure **2** exhibits a 50% compositional disorder between the Br(1) and I(1) sites (Figure 2b), revealing a 1:1 mixture of constitutional isomers of **2** based on the connectivity of the binaphthyl group to the triphenylene core at positions C(1) and C(2).

The hierarchical on-surface growth protocol was implemented in four steps. Step I: Molecular precursors **1**–**3** were sequentially deposited onto a clean Au(111) substrate (**1** and **3** were deposited in excess relative to **2**). Step II: The surface temperature was raised to $T_1$ in order to induce the homolytic cleavage of the C–I bonds in **1** and **2**, thus leading to the formation of linear chains of *poly*-**1** terminated by the linker molecule **2** (*poly*-**1**-**2** in Figure 1b). Step III: The surface temperature was raised further to $T_2$ in order to activate the C–Br bonds in **2** and **3**, thus extending the polymer chains from the ends of *poly*-**1**-**2**. The monomer sequence in the resulting block copolymer (Figure 1c) determines the segmentation of the GNR heterostructure. Step IV: The surface temperature was raised to $T_3$ to induce the cyclodehydrogenation reaction, leading to fully extended GNRs featuring a single in-line heterojunction (Figure 1d).

Scanning tunneling microscopy (STM) imaging was used to follow the experimental implementation of this growth protocol. Figure 3a–c depicts the results of Step I. Figure 3a shows the Au(111) surface after deposition of **1**, while Figure 3b shows the surface after additional deposition of small amounts of **2**. The molecular precursors cluster along the Au(111) herringbone reconstruction. The apparent height of **2** (4.9 Å) is significantly larger than the height of **1** (2.6 Å) due to the nonplanar arrangement of the binaphthyl group in **2**. This unique structural feature allows a clear distinction between monomers of **1** and **2** on the surface. Figure 3c shows an STM image of the surface following the additional deposition of **3**.

Steps II and III were performed by gradually increasing the temperature of the surface to 200 °C at a rate of 2 K min$^{-1}$. Figure 3d shows an STM image of the resulting polymers self-assembled into ordered islands, similar to the polymer stage for pure cGNRs.[15,36] The polymers exhibit segments with different apparent heights, thus allowing taller binaphthyl-containing segments to be distinguished from other chevron polymer segments (see close-up in Figure 3e). A structural model in

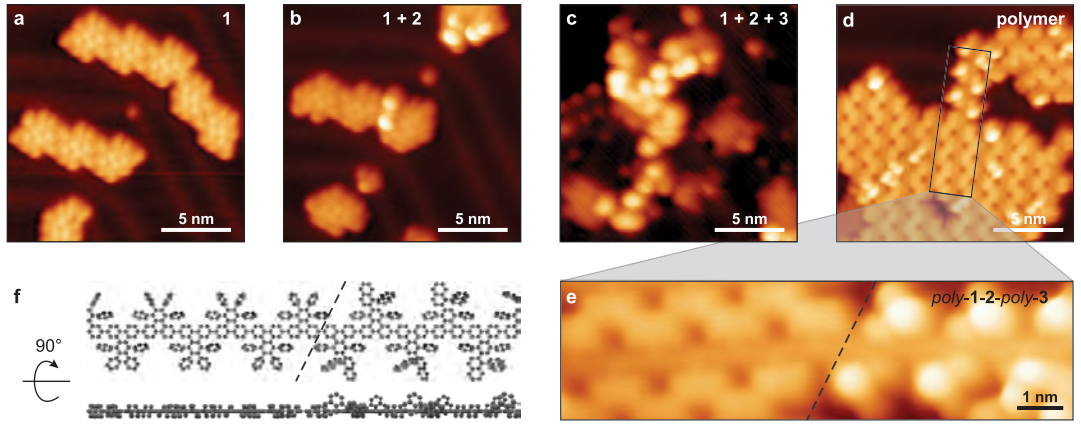


**Figure 3. Hierarchical on-surface copolymerization. (a) STM topograph of 1 adsorbed on Au(111) ($V$ = 1.5 V, $I$ = 20 pA). (b) 1 and 2 co-adsorbed on Au(111) ($V$ = 1.5 V, $I$ = 20 pA). Taller protrusions correspond to 2. (c) 1, 2, and 3 co-adsorbed on Au(111) ($V$ = 1.5 V, $I$ = 20 pA). (d) Island of copolymers on Au(111) after annealing to 200 °C ($V$ = 1.0 V, $I$ = 20 pA). (e) Zoom-in of copolymer outlined in (d) ($V$ = 1.0 V, $I$ = 20 pA). (f) Top-down and side-on view of a molecular model for the copolymer depicted in (e).**



DOI: 10.1021/acsnano.7b08658
*ACS Nano* 2018, 12, 2193–2200

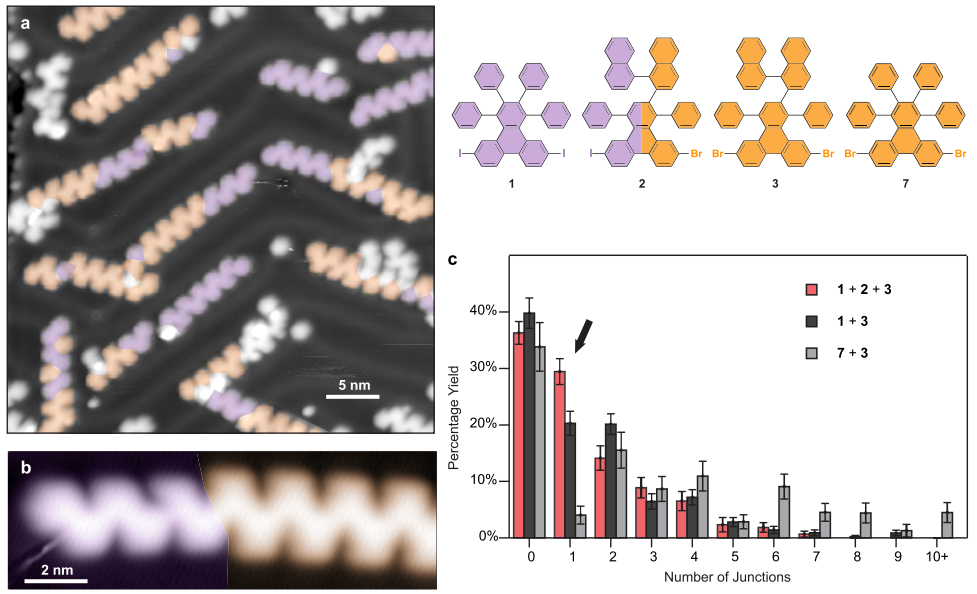


**Figure 4. Hierarchically grown GNR heterojunctions. (a) STM image of cGNR/binaph-cGNR heterojunctions ($V$ = 0.3 V, $I$ = 20 pA). cGNR (binaph-cGNR) segments are highlighted in purple (orange). (b) Magnified STM image of a GNR heterojunction ($V$ = 0.3 V, $I$ = 20 pA). (c) Relative occurrence of GNRs containing different numbers of heterojunctions upon synthesis from precursors 1−3 ("full hierarchical protocol", red), 1 and 3 ("partial hierarchical protocol", dark gray), and 7 and 3 ("random protocol", light gray). The black arrow emphasizes the increase in single-junction GNR heterostructures arising from hierarchical growth.**

Figure 3f illustrates the binaphthyl groups protruding from the molecular plane.

Step IV was accomplished by ramping the sample temperature to 340 °C. As seen in Figure 4a, this results in isolated GNRs comprised of fully cyclized cGNR and binaph-cGNR segments joined in heterojunction structures. STM topography of the segmented GNRs shows a preferred alignment with the herringbone reconstruction and a uniform apparent height of 2.2 Å, lower than the polymers and consistent with previous GNR measurements.[15,16] While the median length of the GNRs was 8 nm, some GNRs exhibited lengths exceeding 20 nm (see Figure S3). cGNR segments and binaph-cGNR segments can clearly be distinguished based on differences in width and shape and are highlighted in purple (from monomer **1**) and orange (from linker **2** and monomer **3**) colors in Figure 4a (see Figure S4 for unprocessed image). Some GNRs can be found on the surface that are comprised of homopolymers of pure chevron or pure binaphthyl building blocks, but most contain a heterojunction. We assign the sporadic occurrence of binaph-cGNRs terminated by cGNR segments to covalent coupling of two block copolymers during step III and a small overlap of the polymerization temperature ranges of iodinated and brominated precursors. We expect that the latter will be less of a problem for other GNR species whose polymerization temperature, unlike the chevron GNRs, is determined more by dehalogenation than by surface diffusion.[36,38]

In order to assess quantitatively whether the hierarchical growth strategy introduced here provides additional control over heterojunction formation compared to random heterojunction synthesis (as performed previously),[23,24] we conducted two control experiments and compared the heterojunction statistics. In the first control experiment (the "partial hierarchical protocol") we synthesized GNR heterostructures by codepositing only **1** and **3** (thus omitting the linker molecule **2**) and then following the same annealing protocol as before. The purpose here was to test the advantage of using the bifunctional linker molecule **2** to cap *poly*-**1** in order to promote single-heterojunction formation. In the second control experiment (the "random protocol") we codeposited the brominated binaphthyl precursor **3** with a conventional brominated cGNR precursor **7** (see Figure 4c) and then followed the same annealing protocol. This second control experiment is essentially the same technique used previously to create random heterojunctions from two different precursors.[23,24]

Figure 4c shows a histogram depicting the relative abundance of GNRs containing a given number of heterojunctions for all three growth protocols (*i.e.*, the full hierarchical growth protocol as well as the two control experiments). A comparison of the three procedures confirms that the full hierarchical growth protocol does indeed result in a significant increase of single-junction GNRs. This effect is largest compared to the random protocol where the relative number of single-junction GNRs is increased by a factor of 7. The full hierarchical growth protocol also results in a 45% increase in single-junction GNRs compared to the partial hierarchical protocol. Overall, hierarchical growth is seen to provide significantly better control over GNR heterojunction synthesis.

It is interesting to note that the random growth protocol (**7** + **3**) results in an overabundance of GNRs containing an even number of heterojunctions, as seen in Figure 4c. The reason for this is that it is common for a cGNR polymer to have isolated binaph-cGNR monomers embedded within it as a result of the random protocol, thus causing two heterojunctions for every isolated binaph-cGNR monomer. This heterojunction scenario likely arises from the lower diffusivity of larger precursor **7** molecules compared to the smaller precursor **3**. Figure 4c shows that this effect is reduced significantly in the partial hierarchical protocol and even more in the full hierarchical protocol due to the increased separation of polymerization temperatures for cGNR and binaph-cGNR precursors in the hierarchical growth schemes.



DOI: 10.1021/acsnano.7b08658
*ACS Nano* 2018, 12, 2193−2200

## ELECTRONIC CHARACTERIZATION OF GNR HETEROJUNCTIONS

The electronic structure of GNR heterojunctions prepared following the hierarchical growth protocol was characterized using a combination of d$I$/d$V$ spectroscopy and density functional theory (DFT) simulations. Figure 5 shows the

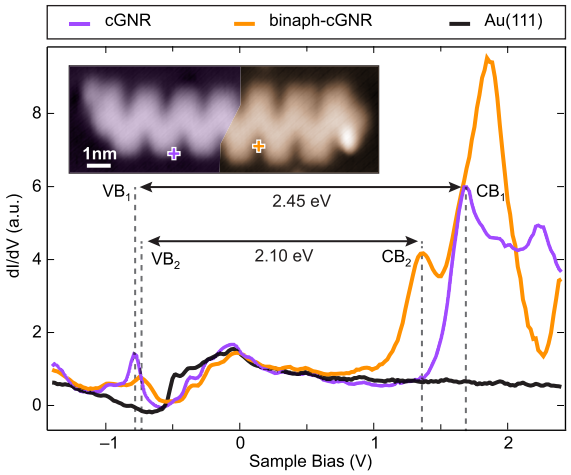


**Figure 5. Spatially inhomogeneous bandgap of cGNR/binaph-cGNR heterojunction. d$I$/d$V$ spectra recorded above the cGNR (purple) and binaph-cGNR (orange) segments of a single-junction GNR compared to the bare Au(111) surface. $VB_{1,2}$ and $CB_{1,2}$ denote the valence and conduction band edges of the cGNR and binaph-cGNR segments, respectively. Inset: STM image showing spectroscopy locations (STS set point: $V$ = 0.3 V, $I$ = 20 pA).**

results of d$I$/d$V$ spectroscopy performed on a narrow cGNR heterojunction segment and a wide binaph-cGNR segment within the single-junction GNR shown in the inset. Both segments exhibit peaks indicative of the energies of the valence band (VB) edge and conduction band (CB) edge of the respective segments. In the cGNR (binaph-cGNR) segment, the VB edge lies at $E_{VB1} = -0.78 \pm 0.03$ eV ($E_{VB2} = -0.74 \pm 0.04$ eV), while the CB edge lies at $E_{CB1} = 1.67 \pm 0.03$ eV ($E_{CB2} = 1.36 \pm 0.02$ eV) with respect to the Fermi level. The resulting bandgap of 2.45 ± 0.05 eV in the cGNR segment agrees well with previous scanning tunneling spectroscopy (STS) experiments[26] and reasonably well with other reported values in the literature ranging from 2.0 to 3.1 eV.[23,35,34] The binaph-cGNR segment, which has not been reported before, features a smaller bandgap of 2.10 ± 0.05 eV. The reduction of the band gap is consistent with the extension of the conjugated $\pi$-system in the binaph-cGNR segment. The straddling band alignment of the two GNR segments defines the heterojunction as Type I.

A characteristic feature of heterojunctions is that band edge wave functions tend to localize on one side of the heterojunction interface.[23] We explored this behavior in hierarchically grown cGNR/binaph-cGNR heterojunctions using d$I$/d$V$ mapping. Figure 6 shows the wave function distribution (*i.e.*, local density of states (LDOS)) across the heterojunction interface for states at the four band edges of the two GNR segments. Spatial localization is clearly observed at the band edges of the binaph-cGNR segment ($CB_2$, $VB_2$) where the wave function appears more intense on the binaph-cGNR side of the interface (Figure 6c,d). Some localization is also seen at the cGNR conduction band edge ($CB_1$) where the wave function is more intense on the cGNR side of the interface

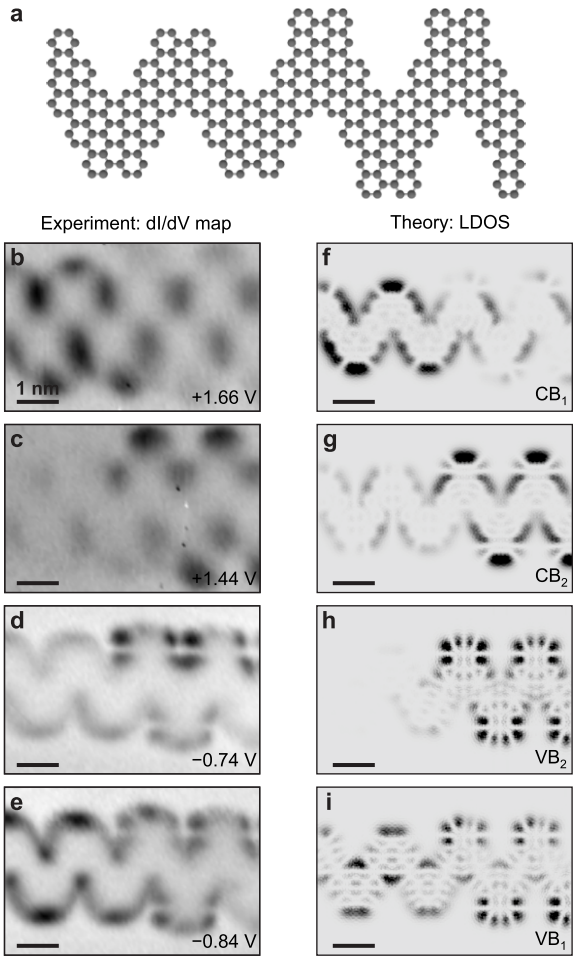


**Figure 6. Spatial distribution of heterojunction band edge states. (a) Molecular model of the GNR heterojunction investigated in (b–i). (b–e) Constant-current d$I$/d$V$ maps of VB and CB edge states for the two heterojunction segments. (f–i) Simulated local density of states associated with VB and CB edge states for the two heterojunction segments calculated using DFT. Black (gray) represents high (low) intensity.**

(Figure 6b). The wave function at the valence band edge of the cGNR ($VB_1$), however, does not show significant localization across the interface (Figure 6e).

In order to test that our experimental cGNR/binaph-cGNR heterojunction behavior is consistent with the expected electronic properties of a GNR heterojunction, we performed *ab initio* simulations of the heterojunction electronic structure using DFT. Figure S5 shows the unit cell used in the calculation. Our simulation confirms the reduced energy gap of the binaph-cGNR segment compared to the cGNR segment and reproduces the Type I heterojunction band alignment seen experimentally (Figure S5). Theoretical simulations of the spatial distribution of the heterojunction LDOS (Figure 6f–i) confirm the wave function localization observed experimentally. Theoretical LDOS maps obtained at the band edge energies of the binaph-cGNR segment ($CB_2$, $VB_2$) show noticeable localization on that side of the heterojunction interface as well as a distinct nodal structure that resembles the experimental LDOS distribution (Figure 6c,d). Like the experiment, the theoretical LDOS distribution at the cGNR conduction band energy ($CB_1$) shows some localization on the cGNR side (Figure 6f), while the LDOS at the cGNR valence



DOI: 10.1021/acsnano.7b08658
*ACS Nano* 2018, 12, 2193–2200

band energy ($VB_1$) shows no discernible localization (Figure 6i). The reduced wave function localization at the cGNR band edges arises from the fact that they are degenerate with states in the binaph-cGNR segment due to the Type I heterojunction band alignment. The band edge states on the binaph-cGNR side ($CB_2$, $VB_2$), by contrast, lie in the cGNR gap and are thus more strongly confined.

## CONCLUSION

We have demonstrated hierarchical on-surface synthesis of GNR heterojunctions from molecular precursors engineered to yield a predetermined growth sequence. This was accomplished by taking advantage of the subtle differences in the bond dissociation energies of C−I bonds compared to C−Br bonds to separate polymerization temperatures for different precursors. We observe that the use of a bifunctional linker molecule (*i.e.*, one that includes both C−I *and* C−Br bonds) leads to single-heterojunction yields that are dramatically improved when compared to more standard uniform precursor functionalization (*i.e.*, the use of exclusively brominated precursors) and also significantly better than a partial hierarchical growth protocol that forgoes the linker. STS measurements on hierarchically grown cGNR/binaph-cGNR heterojunctions reveal a Type I band alignment with strong wave function localization for the bands closest to the Fermi energy, consistent with *ab initio* simulations. The improved GNR heterojunction structural control demonstrated here for hierarchical growth techniques should help facilitate the integration of atomically precise GNR heterostructures into future nanoelectronic devices.

## METHODS

**Precursor Synthesis.** Full details regarding the synthesis and characterization of all precursor materials are given in the Supporting Information.

**STM Measurements.** The on-surface reactions were conducted on a clean Au(111) single crystal which was prepared by cycles of $Ar^+$ sputtering and annealing. All precursor molecules were evaporated from homemade Knudsen cells. The Knudsen cell sublimation temperatures of the precursors were 170 °C (**1**), 200 °C (**2**), 165 °C (**3**), and 160 °C (**7**). The monomers were deposited onto the substrate while holding it at $T < -50$ °C (the sample was taken directly from the cryogenic STM stage just prior to evaporation). STM imaging was performed in constant-current mode using a home-built STM at a temperature of $T = 13$ K. Differential conductance ($dI/dV$) measurements were recorded using a lock-in amplifier with modulation frequency of 566 Hz and modulation amplitude $V_{rms}$ = 10−25 mV. $dI/dV$ point spectra were recorded under open feedback loop conditions. $dI/dV$ maps were collected under constant-current conditions.

**Calculations.** Theoretical simulations of freestanding GNR heterojunctions were performed using DFT within the local density approximation (LDA) as implemented in the Quantum Espresso package.[39] A supercell with sufficient vacuum space (>10 Å) was used to avoid spurious interaction between periodic replicas. We used norm-conserving pseudopotentials with a planewave energy cutoff of 60 Ry. The heterojunction structure was fully relaxed until the force on each atom was smaller than 0.025 eV/Å. All edges were saturated with hydrogen atoms. A Gaussian broadening of 0.08 eV was used in the LDOS calculations.

## ASSOCIATED CONTENT

### Supporting Information

The Supporting Information is available free of charge on the ACS Publications website at DOI: 10.1021/acsnano.7b08658.

Crystallographic data (CIF)

Control experiments using the "partial hierarchical" and "random" protocols; analysis of the GNR's length distribution; unprocessed image of Figures 4a,b; DFT calculation of the projected density of states near a GNR heterojunction; synthesis and characterization of the molecular precursors (PDF)

## AUTHOR INFORMATION


### Corresponding Authors

*E-mail: bronner@berkeley.edu.
*E-mail: ffischer@berkeley.edu.
*E-mail: crommie@berkeley.edu.

### ORCID

Christopher Bronner: 0000-0002-0083-5089
Felix R. Fischer: 0000-0003-4723-3111
Michael F. Crommie: 0000-0001-8246-3444


### Author Contributions

#These authors contributed equally. C.B., R.A.D., M.F.C., and F.R.F. conceived the experiments; R.A.D., T.M., and A.M.K. designed, synthesized, and characterized the molecular precursors; C.B., D.J.R., H.R., and W.Z. performed the on-surface synthesis and STM characterization; Y.-L. L. and S.G.L. performed and interpreted the DFT calculations; and C.B., R.A.D., D.J.R., Y.-L. L., S.G.L., F.R.F., and M.F.C. wrote the manuscript. All authors contributed to the scientific discussion.

### Notes

The authors declare no competing financial interest.

## ACKNOWLEDGMENTS

Research supported by the Office of Naval Research MURI Program N00014-16-1-2921 (precursor design, surface growth, STM imaging, band structure), by the U.S. Department of Energy (DOE), Office of Science, Basic Energy Sciences (BES) under the Nanomachine Program award no. DE-AC02-05CH11231 (STM spectroscopy and simulation) and award no. DE-SC0010409 (precursor synthesis and characterization), by the Center for Energy Efficient Electronics Science NSF Award 0939514 (heterojunction modelling), and by the National Science Foundation under grant DMR-1508412 (development of theory formalism). Computational resources have been provided by the DOE at Lawrence Berkeley National Laboratory's NERSC facility and by the NSF through XSEDE resources at NICS. C.B. acknowledges support through the Fellowship Program of the German National Academy of Sciences Leopoldina under grant no. LPDS 2014-09.

## REFERENCES


(1) Tanaka, K.; Yamashita, S.; Yamabe, H.; Yamabe, T. Electronic Properties of One-Dimensional Graphite Family. *Synth. Met.* **1987**, *17*, 143−148.

(2) Barone, V.; Hod, O.; Scuseria, G. E. Electronic Structure and Stability of Semiconducting Graphene Nanoribbons. *Nano Lett.* **2006**, *6*, 2748−2754.

(3) Ezawa, M. Peculiar Width Dependence of the Electronic Properties of Carbon Nanoribbons. *Phys. Rev. B: Condens. Matter Mater. Phys.* **2006**, *73*, 045432.

(4) Son, Y.-W.; Cohen, M. L.; Louie, S. G. Energy Gaps in Graphene Nanoribbons. *Phys. Rev. Lett.* **2006**, *97*, 216803.

(5) Yang, L.; Park, C.-H.; Son, Y.-W.; Cohen, M. L.; Louie, S. G. Quasiparticle Energies and Band Gaps in Graphene Nanoribbons. *Phys. Rev. Lett.* **2007**, *99*, 186801.




DOI: 10.1021/acsnano.7b08658
*ACS Nano* 2018, 12, 2193−2200

(6) Bennett, P. B.; Pedramrazi, Z.; Madani, A.; Chen, Y.-C.; de Oteyza, D. G.; Chen, C.; Fischer, F. R.; Crommie, M. F.; Bokor, J. Bottom-Up Graphene Nanoribbon Field-Effect Transistors. *Appl. Phys. Lett.* **2013**, *103*, 253114.
(7) Llinas, J. P.; Fairbrother, A.; Borin Barin, G.; Shi, W.; Lee, K.; Wu, S.; Choi, B. Y.; Braganza, R.; Lear, J.; Kau, N.; Choi, W.; Chen, C.; Pedramrazi, Z.; Dumslaff, T.; Narita, A.; Feng, X.; Müllen, K.; Fischer, F.; Zettl, A.; Ruffieux, P.; Yablonovitch, E.; Crommie, M.; Fasel, R.; Bokor, J. Short-Channel Field-Effect Transistors with 9-Atom and 13-Atom Wide Graphene Nanoribbons. *Nat. Commun.* **2017**, *8*, 633.
(8) Yoon, Y.; Salahuddin, S. Barrier-Free Tunneling in a Carbon Heterojunction Transistor. *Appl. Phys. Lett.* **2010**, *97*, 033102.
(9) Yoon, Y.; Salahuddin, S. Dissipative Transport in Rough Edge Graphene Nanoribbon Tunnel Transistors. *Appl. Phys. Lett.* **2012**, *101*, 263501.
(10) Nakada, K.; Fujita, M.; Dresselhaus, G.; Dresselhaus, M. S. Edge State in Graphene Ribbons: Nanometer Size Effect and Edge Shape Dependence. *Phys. Rev. B: Condens. Matter Mater. Phys.* **1996**, *54*, 17954.
(11) Han, M. Y.; Özyilmaz, B.; Zhang, Y.; Kim, P. Energy Band-Gap Engineering of Graphene Nanoribbons. *Phys. Rev. Lett.* **2007**, *98*, 206805.
(12) Li, X.; Wang, X.; Zhang, L.; Lee, S.; Dai, H. Chemically Derived, Ultrasmooth Graphene Nanoribbon Semiconductors. *Science* **2008**, *319*, 1229−1232.
(13) Kosynkin, D. V.; Higginbotham, A. L.; Sinitskii, A.; Lomeda, J. R.; Dimiev, A.; Price, B. K.; Tour, J. M. Longitudinal Unzipping of Carbon Nanotubes to Form Graphene Nanoribbons. *Nature* **2009**, *458*, 872−876.
(14) Jiao, L.; Zhang, L.; Wang, X.; Diankov, G.; Dai, H. Narrow Graphene Nanoribbons from Carbon Nanotubes. *Nature* **2009**, *458*, 877−880.
(15) Cai, J.; Ruffieux, P.; Jaafar, R.; Bieri, M.; Braun, T.; Blankenburg, S.; Muoth, M.; Seitsonen, A. P.; Saleh, M.; Feng, X.; Müllen, K.; Fasel, R. Atomically Precise Bottom-Up Fabrication of Graphene Nanoribbons. *Nature* **2010**, *466*, 470−473.
(16) Chen, Y.-C.; de Oteyza, D. G.; Pedramrazi, Z.; Chen, C.; Fischer, F. R.; Crommie, M. F. Tuning the Band Gap of Graphene Nanoribbons Synthesized from Molecular Precursors. *ACS Nano* **2013**, *7*, 6123−6128.
(17) Sakaguchi, H.; Kawagoe, Y.; Hirano, Y.; Iruka, T.; Yano, M.; Nakae, T. Width-Controlled Sub-Nanometer Graphene Nanoribbon Films Synthesized by Radical-Polymerized Chemical Vapor Deposition. *Adv. Mater.* **2014**, *26*, 4134−4138.
(18) Kimouche, A.; Ervasti, M. M.; Drost, R.; Halonen, S.; Harju, A.; Joensuu, P. M.; Sainio, J.; Liljeroth, P. Ultra-Narrow Metallic Armchair Graphene Nanoribbons. *Nat. Commun.* **2015**, *6*, 10177.
(19) Han, P.; Akagi, K.; Federici Canova, F.; Mutoh, H.; Shiraki, S.; Iwaya, K.; Weiss, P. S.; Asao, N.; Hitosugi, T. Bottom-Up Graphene-Nanoribbon Fabrication Reveals Chiral Edges and Enantioselectivity. *ACS Nano* **2014**, *8*, 9181−9187.
(20) Ruffieux, P.; Wang, S.; Yang, B.; Sánchez-Sánchez, C.; Liu, J.; Dienel, T.; Talirz, L.; Shinde, P.; Pignedoli, C. A.; Passerone, D.; Dumslaff, T.; Feng, X.; Müllen, K.; Fasel, R. On-Surface Synthesis of Graphene Nanoribbons with Zigzag Edge Topology. *Nature* **2016**, *531*, 489−492.
(21) Talirz, L.; Söde, H.; Dumslaff, T.; Wang, S.; Sanchez-Valencia, J. R.; Liu, J.; Shinde, P.; Pignedoli, C. A.; Liang, L.; Meunier, V.; Plumb, N. C.; Shi, M.; Feng, X.; Narita, A.; Müllen, K.; Fasel, R.; Ruffieux, P. On-Surface Synthesis and Characterization of 9-Atom Wide Armchair Graphene Nanoribbons. *ACS Nano* **2017**, *11*, 1380−1388.
(22) Liu, J.; Li, B.-W.; Tan, Y.-Z.; Giannakopoulos, A.; Sanchez-Sanchez, C.; Beljonne, D.; Ruffieux, P.; Fasel, R.; Feng, X.; Müllen, K. Toward Cove-Edged Low Band Gap Graphene Nanoribbons. *J. Am. Chem. Soc.* **2015**, *137*, 6097−6103.
(23) Cai, J.; Pignedoli, C. A.; Talirz, L.; Ruffieux, P.; Söde, H.; Liang, L.; Meunier, V.; Berger, R.; Li, R.; Feng, X.; Müllen, K.; Fasel, R. Graphene Nanoribbon Heterojunctions. *Nat. Nanotechnol.* **2014**, *9*, 896−900.
(24) Chen, Y.-C.; Cao, T.; Chen, C.; Pedramrazi, Z.; Haberer, D.; de Oteyza, D. G.; Fischer, F. R.; Louie, S. G.; Crommie, M. F. Molecular Bandgap Engineering of Bottom-Up Synthesized Graphene Nanoribbon Heterojunctions. *Nat. Nanotechnol.* **2015**, *10*, 156−160.
(25) Marangoni, T.; Haberer, D.; Rizzo, D. J.; Cloke, R. R.; Fischer, F. R. Heterostructures through Divergent Edge Reconstruction in Nitrogen-Doped Segmented Graphene Nanoribbons. *Chem. - Eur. J.* **2016**, *22*, 13037−13040.
(26) Nguyen, G. D.; Tsai, H.-Z.; Omrani, A. A.; Marangoni, T.; Wu, M.; Rizzo, D. J.; Rodgers, G. F.; Cloke, R. R.; Durr, R. A.; Sakai, Y.; Liou, F.; Aikawa, A. S.; Chelikowsky, J. R.; Louie, S. G.; Fischer, F. R.; Crommie, M. F. Atomically Precise Graphene Nanoribbon Heterojunctions from a Single Molecular Precursor. *Nat. Nanotechnol.* **2017**, *12*, 1077−1082.
(27) Lafferentz, L.; Eberhardt, V.; Dri, C.; Africh, C.; Comelli, G.; Esch, F.; Hecht, S.; Grill, L. Controlling On-Surface Polymerization by Hierarchical and Substrate-Directed Growth. *Nat. Chem.* **2012**, *4*, 215−220.
(28) Steiner, C.; Gebhardt, J.; Ammon, M.; Yang, Z.; Heidenreich, A.; Hammer, N.; Görling, A.; Kivala, M.; Maier, S. Hierarchical On-Surface Synthesis and Electronic Structure of Carbonyl-Functionalized One- and Two-Dimensional Covalent Nanoarchitectures. *Nat. Commun.* **2017**, *8*, 14765.
(29) Simonov, K. A.; Vinogradov, N. A.; Vinogradov, A. S.; Generalov, A. V.; Zagrebina, E. M.; Mårtensson, N.; Cafolla, A. A.; Carpy, T.; Cunniffe, J. P.; Preobrajenski, A. B. Effect of Substrate Chemistry on the Bottom-Up Fabrication of Graphene Nanoribbons: Combined Core-Level Spectroscopy and STM Study. *J. Phys. Chem. C* **2014**, *118*, 12532−12540.
(30) Batra, A.; Cvetko, D.; Kladnik, G.; Adak, O.; Cardoso, C.; Ferretti, A.; Prezzi, D.; Molinari, E.; Morgante, A.; Venkataraman, L. Probing the Mechanism for Graphene Nanoribbon Formation on Gold Surfaces through X-Ray Spectroscopy. *Chem. Sci.* **2014**, *5*, 4419−4423.
(31) Syomin, D.; Koel, B. E. Adsorption of iodobenzene ($C_6H_5I$) on Au(1 1 1) Surfaces and Production of Biphenyl ($C_6H_5-C_6H_5$). *Surf. Sci.* **2001**, *490*, 265−273.
(32) Bieri, M.; Nguyen, M.-T.; Gröning, O.; Cai, J.; Treier, M.; Aït-Mansour, K.; Ruffieux, P.; Pignedoli, C. A.; Passerone, D.; Kastler, M.; Müllen, K.; Fasel, R. Two-Dimensional Polymer Formation on Surfaces: Insight into the Roles of Precursor Mobility and Reactivity. *J. Am. Chem. Soc.* **2010**, *132*, 16669−16676.
(33) Eichhorn, J.; Nieckarz, D.; Ochs, O.; Samanta, D.; Schmittel, M.; Szabelski, P. J.; Lackinger, M. On-Surface Ullmann Coupling: The Influence of Kinetic Reaction Parameters on the Morphology and Quality of Covalent Networks. *ACS Nano* **2014**, *8*, 7880−7889.
(34) Linden, S.; Zhong, D.; Timmer, A.; Aghdassi, N.; Franke, J. H.; Zhang, H.; Feng, X.; Müllen, K.; Fuchs, H.; Chi, L.; Zacharias, H. Electronic Structure of Spatially Aligned Graphene Nanoribbons on Au(788). *Phys. Rev. Lett.* **2012**, *108*, 216801.
(35) Bronner, C.; Stremlau, S.; Gille, M.; Brauße, F.; Haase, A.; Hecht, S.; Tegeder, P. Aligning the Band Gap of Graphene Nanoribbons by Monomer Doping. *Angew. Chem., Int. Ed.* **2013**, *52*, 4422−4425.
(36) Bronner, C.; Marangoni, T.; Rizzo, D. J.; Durr, R. A.; Holm Jørgensen, J.; Fischer, F. R.; Crommie, M. F. Iodine *versus* Bromine Functionalization for Bottom-Up Graphene Nanoribbon Growth: Role of Diffusion. *J. Phys. Chem. C* **2017**, *121*, 18490−18495.
(37) Thiessen, A.; Wettach, H.; Meerholz, K.; Neese, F.; Höger, S.; Hertel, D. Control of Electronic Properties of Triphenylene by Substitution. *Org. Electron.* **2012**, *13*, 71−83.
(38) Di Giovannantonio, M.; Deniz, O.; Urgel, J. I.; Widmer, R.; Dienel, T.; Stolz, S.; Sánchez-Sánchez, C.; Muntwiler, M.; Dumslaff, T.; Berger, R.; Narita, A.; Feng, X.; Müllen, K.; Ruffieux, P.; Fasel, R. On-Surface Growth Dynamics of Graphene Nanoribbons: The Role of Halogen Functionalization. *ACS Nano* **2018**, *12*, 74−81.
(39) Giannozzi, P.; Baroni, S.; Bonini, N.; Calandra, M.; Car, R.; Cavazzoni, C.; Ceresoli, D.; Chiarotti, G. L.; Cococcioni, M.; Dabo, I.; Dal Corso, A.; de Gironcoli, S.; Fabris, S.; Fratesi, G.; Gebauer, R.;


DOI: 10.1021/acsnano.7b08658
*ACS Nano* 2018, 12, 2193−2200

Gerstmann, U.; Gougoussis, C.; Kokalj, A.; Lazzeri, M.; Martin-Samos, L.; et al. QUANTUM ESPRESSO: A Modular and Open-Source Software Project for Quantum Simulations of Materials. *J. Phys.: Condens. Matter* **2009**, *21*, 395502.



DOI: 10.1021/acsnano.7b08658
*ACS Nano* 2018, 12, 2193−2200